Journal of Non-Newtonian Fluid Mechanics 234 (2016) 118–128

Contents lists available at ScienceDirect

Journal of Non-Newtonian Fluid Mechanics

journal homepage: www.elsevier.com/locate/jnnfm

Lattice Boltzmann modeling for multiphase viscoplastic fluid flow

Chiyu Xie[a], Jianying Zhang[b], Volfango Bertola[c], Moran Wang[a,*]

[a] Department of Engineering Mechanics and CNMM, Tsinghua University, Beijing 100084, China
[b] College of Engineering, Peking University, Beijing 100874, China
[c] School of Engineering, University of Liverpool, Brownlow Hill, Liverpool L69 3GH, UK

ARTICLE INFO

Article history:
Received 23 November 2015
Revised 11 May 2016
Accepted 13 May 2016
Available online 20 May 2016

Keywords:
Viscoplastic fluid
Multiphase flow
Herschel-Bulkley model
Lattice Boltzmann method

ABSTRACT

We present a lattice Boltzmann model to simulate multiphase viscoplastic fluid flow. It is an extended model based on the free-energy-based lattice Boltzmann method (LBM) for multiphase fluids with possible high-density and high-viscosity ratios by applying the Herschel-Bulkley constitutive relationship to account for the variable viscosity. The model shows good agreements between the simulation results and the corresponding theoretical solutions for different cases. Furthermore, the capability and effectivity of this model is tested by examples, including droplet(s) falling and interaction in Bingham fluid, and sessile viscoplastic droplet motion. The results illustrate that our model is able to catch the yield behavior well, and to distinguish various kinds of viscoplastic fluids effectively.

1. Introduction

Viscoplastic materials, or viscoplastic fluids, represent one of the most important categories of non-Newtonian fluids. Their most important feature is the existence of a critical stress value, known as the yield stress [1]. When the stress inside the material exceeds this value, the material will yield and begin to flow as a fluid; while if the inner stress is below this value, the material will be un-yielded and behave like a solid. Hence viscoplastic fluids are also termed as yield stress fluids [1]. Viscoplastic fluids are common in everyday life, such as toothpaste, mud, cements, food, etc. Moreover, interaction of a viscoplastic fluid with another fluid is of essential importance in fields like biotechnology [2,3], chemical engineering [4], and petroleum industry [5,6].

For the general problem of multiphase viscoplastic fluid flow, numerous studies have been carried out and summarized in a comprehensive review [7]. Comparini & Mannucci [8] theoretically solved the flow of a Bingham fluid (the simplest viscoplastic fluid) in contact with a Newtonian fluid. Frigaard [9] derived a series of non-dimensional theoretical solutions for parallel multiphase Bingham flow. Experimentally, bubble(s) rising [10–12] and droplet(s) motion [13,14] in a viscoplastic fluid, as well as formation [15–17] and impact of viscoplastic droplet(s) [18] were widely investigated. Numerically, a variety of methods were applied, including the finite volume method [19], the finite element method [20–22], the augmented Lagrangian method [23], the integral equation method [24], and so on. However, there still remain many challenges in simultaneously dealing with the complexity of interfacial dynamics and the nonlinearity of viscoplastic fluids efficiently [25].

Since 1990 s, the lattice Boltzmann method (LBM) has offered an alternative powerful way for fluid dynamic simulations [26,27]. It is a mesoscopic method embedding kinetic features [28]. In comparison with the traditional CFD methods, the greatest strength of LBM is the capability of efficiently solving various kinds of complicated fluid transport phenomena coupled with electro-kinetics, magnetics, thermodynamics, etc. [29–34]. Several LBM models have been developed for multiphase flow and interfacial dynamics [35]. The color-fluid model [36–39] was first proposed in 1988 by using a compulsive “recolor” step to separate different phases. In 1993, Shan & Chen proposed the pseudo-potential model [40] by introducing an inter-particle potential force to guarantee the phase separation. Later, the free-energy model [41] and the mean-field model [42,43] were proposed in 1995 and 1998 respectively. However, because of the challenges in dealing with the sharp density transition across the interface, all of these early models suffer from the small density-ratio limit. In order to remove this drawback, a number of improved models emerged. Major parts of these models introduced the phase-field method [44–46] to capture the interface, which adopted the concept of free-energy that assures thermodynamic consistency and offers deeper physical understandings [47,48]. By using the projection method to decouple the velocity and pressure fields, Inamuro et al. [49] proposed a model that allows density-ratios up to 1000. However, multiple sets of lattice Boltzamnn equations induced by the projection procedure made the Inamuro’s model lose the efficient feature of LBM. Lee & Lin [50] introduced a model based on the mean-field model, and it was further improved to account for wetting boundaries [51,52]. This model was available to accurately capture the large

* Corresponding author.
E-mail address: mrwang@tsinghua.edu.cn (M. Wang).

http://dx.doi.org/10.1016/j.jnnfm.2016.05.003
0377-0257/

density-ratio multiphase fluid dynamics; however, the numerous exact differential schemes in this model reduced the efficiency significantly. Zheng et al. [53] presented another model applicable for large density ratios (ZSC model) by using the mean density for hydrodynamic evolutions. This model has been developed to study the evaporation of a droplet [54]. Compared with the former models, it is of higher efficiency. Since the mean density was used, it could not correctly catch the momentum exchange in multiphase systems [55,56]. This drawback was removed by Shao et al. [56] recently with preserved efficiency.

Meanwhile, many efforts have been made to account for non-Newtonian behaviors [57]. Gabbanelli et al. [58] employed a truncated power-law model to simulate power-law flow between parallel plates. Boyd et al. [59] improved the accuracy of LBM model for power-law fluids to the second order. Pontrelli et al. [60] proposed an unstructured power-law LBM model by using a cell-vertex finite-volume technique. Chen et al. [61] investigated electrokinetic flow of power-law fluids in porous media. Ispolatov & Grant [62] and Lallemand et al. [63] developed 2D and 3D LBM models for viscoelastic fluid respectively. Ohta et al. [64] studied viscoplastic fluid flows through complex channels with circular obstacles. Vikhansky [65] and Derksen [66] applied LBM models to describe the yielded region of Bingham fluid. It is worth mentioning that most of the above LBM approaches only need the local-lattice information to calculate the shear rate, which avoids the complex differential processes in usual CFD methods.

Nevertheless, contributions on combinations of multiphase flow and non-Newtonian fluids in the LBM framework are still rare. Some early models were developed for multiphase viscoelastic fluids: Frank & Li [67,68] employed the free-energy model; Onishi's model [69] originated from the pseudo-potential model, and Yoshino's model [70] was based on Inamuro's model. Later, droplet formation in power-law fluids [71] and fluid displaced by power-law fluids in porous media [72] were investigated, respectively. However, the LBM model considering yield stress or viscoplastic fluids has seldom been reported, until very recently, Swain et al. [73] embedded the yield stress fluids model into the mean-field multiphase LB model proposed by He et al. [42,43] to study the liquid-liquid interaction with limited density ratios and the displacements of a viscoplastic material by a Newtonian fluid.

The objective of this work is to develop a robust multiphase LB model for any viscoplastic fluids with possible high density ratio or high viscosity ratio. It is worth mentioning that we happened to find Swain's work after our work was done, with similar strategy but different methods. In this paper, the LBM scheme is based on the phase-field method for multiphase flow modeling with the capability to cover high density or viscosity ratios. The Herschel-Bulkley model is adopted for the description of viscoplastic fluids. Several cases will be proposed to validate the numerical framework strictly and to examine the accuracy and robustness for any combination of non-Newtonian fluids or density ratios. The paper is organized as follows. Section 2 introduces the fundamental multiphase LBM scheme as well as the phase-field method, and then the extended model to simulate multiphase viscoplastic flows. In Section 3, the basic multiphase LBM code and the present model are verified in a number of cases where exact analytical solutions are available. Section 4 discusses the accuracy and effectivity of this model further by various examples. Finally, we conclude our work in Section 5.

2. Numerical methods

2.1. Multiphase LBM scheme based on phase-field method

For single-phase fluid flow simulation, the continuity equation and the Navier–Stokes equations are sufficient to ensure the mass and momentum conservation. When it comes to multiphase flow, an additional equation is required to capture the interface evolution. The best known interface tracking methods include the volume of fluid method [74], the level-set method [75,76] and the phase-field method [44–46]. Nowadays, the phase-field method is gaining much popularity since it origins from the energy point of view, and provides a better physical understanding. It is a diffuse interface method [77], which looks upon those "discontinuous" interface phenomena in a continuous way. An order parameter is introduced to distinguish each phase; this parameter changes drastically at the interface while keeping the continuity, and leads to the smooth transition of physical parameters. The Cahn-Hilliard equation is the governing equation of the phase-field method, which drives the multiphase system toward its lowest free energy state spontaneously. The general form is expressed as

$$\partial_t \phi + \boldsymbol{u} \cdot \nabla \phi = M \nabla^2 \mu, \tag{1}$$

where $\boldsymbol{u}$ is velocity vector and t is time, ϕ is the order parameter, μ is the chemical potential, and M is the mobility which controls the diffusion rate of interface [78].

According to the ZSC model [53], the Cahn-Hilliard equation can be solved by the LBM equation,

$$g_i(\boldsymbol{x} + \boldsymbol{c_i}\Delta t, t + \Delta t) - g_i(\boldsymbol{x}, t) = -\frac{1}{\tau_g}\left(g_i(\boldsymbol{x}, t) - g_i^{eq}(\boldsymbol{x}, t)\right), \tag{2}$$

where $\boldsymbol{x}$ is lattice position, Δt is the time step, $\boldsymbol{c_i}$ is the lattice velocity with the discrete direction of i, and $\Delta x = \boldsymbol{c_i}\Delta t$ is the lattice size per unit; g_i and g_i^{eq} are, respectively, the distribution function and the corresponding equilibrium distribution function related to ϕ; τ_g is the relaxation parameter of g. When a D2Q9 or a D3Q15 lattice velocity model is used, the equilibrium distribution function g_i^{eq} is given as

$$g_i^{eq}(\boldsymbol{x}, t) = \omega_i\left(B_i + \phi\frac{3\boldsymbol{c_i}\cdot\boldsymbol{u}}{c^2}\right) \tag{3a}$$

$$B_i = \begin{cases} 3\tilde{M}\mu/c^2 = B, & i > 0 \\ [\phi - (1-\omega_0)B]/\omega_0, & i = 0 \end{cases}, \tag{3b}$$

where the parameter $\tilde{M}$ is determined by M and τ_g as

$$\tilde{M} = M/[(\tau_g - 0.5)\Delta t]. \tag{4}$$

Then, using the following correlation between the distribution functions and macroscopic parameters, the Cahn-Hilliard Eq. (1) is recovered with a second order of accuracy by Chapman-Enskog expansion procedure.

$$\sum_i g_i = \sum_i g_i^{eq} = \phi = (\rho_1 - \rho_2)/2 \tag{5a}$$

$$\sum_i g_i^{eq} c_{i\alpha} c_{i\beta} = \tilde{M}\mu\delta_{\alpha\beta}, \tag{5b}$$

where $\delta_{\alpha\beta}$ is the Kronecker delta, the subscripts α, β are the spatial coordinates; ρ_1 and ρ_2 are the density of two fluids.

In the ZSC model, the order parameter related to density difference is adapted to capture the interface, and the mean density is adapted to evolve for the fluid dynamics. Since the mean density is used, this model is more efficient, but the momentum of either fluid is not accurate.

In order to remove this drawback, Shao et al. [56] revised the momentum equation in the original ZSC model as

$$f_i(\boldsymbol{x} + \boldsymbol{c_i}\Delta t, t + \Delta t) - f_i(\boldsymbol{x}, t) = -\frac{1}{\tau_f}\left(f_i(\boldsymbol{x}, t) - f_i^{eq}(\boldsymbol{x}, t)\right) + \Omega_f{}' \tag{6a}$$

$$\Omega_f' = \left(1 - \frac{1}{2\tau_f}\right)\frac{3\Delta t\omega_i}{c^2} \times (\boldsymbol{c_i} - \boldsymbol{u}) \cdot \times \left[\nabla\left(\frac{\rho c^2}{3}\right)\Gamma_i + (-\phi\nabla\mu + \boldsymbol{F})(1+\Gamma_i)\right] \tag{6b}$$

$$\Gamma_i = \frac{3\boldsymbol{c_i}\cdot\boldsymbol{u}}{c^2} + \frac{9(\boldsymbol{c_i}\cdot\boldsymbol{u})^2}{2c^4} - \frac{3\boldsymbol{u}\cdot\boldsymbol{u}}{c^2} \tag{6c}$$

where $\boldsymbol{F}$ is the body force; ρ is the local density; f_i and f_i^{eq} are, respectively, the distribution function and the corresponding equilibrium distribution function related to the mean density ρ_0; τ_f is the relaxation parameter of f. In the framework of D2Q9 or D3Q15 lattice velocity model, the equilibrium distribution function f_i^{eq} is given as

$$f_i^{eq} = \omega_i(\rho_0 + \rho\Gamma_i). \tag{7}$$

The relationships between the distribution functions and macroscopic parameters are

$$\sum_i f_i^{eq} + \Delta t u_\alpha \nabla_\alpha \rho/2 = \rho_0 = (\rho_1 + \rho_2)/2 \tag{8a}$$

$$\sum_i f_i^{eq} c_{i\alpha} + (-\phi\nabla\mu + F_\alpha)/2 = \rho u_\alpha. \tag{8b}$$

Thereafter, using the Chapman-Enskog expansion, the real continuous equation and Navier-Stokes equation for two-phase flow are recovered as

$$\nabla(\rho\boldsymbol{u}) = 0, \tag{9}$$

and

$$\partial_t(\rho\boldsymbol{u}) + \nabla(\rho\boldsymbol{u}u) = -\nabla\left(\rho_0 c^2/3\right) + \rho\nu\Delta\boldsymbol{u} - \phi\nabla\mu + \boldsymbol{F} \tag{10}$$

where ν is the local kinematic viscosity.

At this point, combing Eq. (2) and Eq. (6), one can simulate two-phase Newtonian flows. However, what if one or both phases are viscoplastic?

2.2. Extension to viscoplastic fluids

In this section, the multiphase LBM scheme is developed to deal with viscoplastic fluids. Among the constitutive relations for viscoplastic fluids, the Herschel-Bulkley model [79] is probably the most common and widely used because of its simplicity and flexibility:

$$\tau < \tau_y: \quad \dot\gamma = 0 \tag{11a}$$

$$\tau \geq \tau_y: \quad \tau = \tau_y + K\cdot\dot\gamma^n, \tag{11b}$$

where τ is the shear stress, $\dot\gamma^n$ is the shear rate; τ_y is the yield stress, K is the consistency index, and n is the flow index. As a special case, when $n = 1$, the model reduces to the simplest viscoplastic fluid (Bingham fluid); while for $n = 1$ and $\tau_y = 0$, it reduces to the Newtonian fluid, and K equals to the dynamic viscosity, correspondingly.

By using Eqs. (11), one can easily derive the apparent kinematic viscosity υ as

$$\tau < \tau_y: \quad \upsilon = \infty \tag{12a}$$

$$\tau \geq \tau_y: \quad \upsilon = \frac{\tau_y}{\rho\dot\gamma} + \frac{K}{\rho}\cdot\dot\gamma^{n-1}. \tag{12b}$$

The apparent kinematic viscosity υ is closely related to the relaxation parameter τ_f in LBM. For the commonly used lattice velocity models, one can write

$$\tau_f = \frac{1}{2} + \frac{3\upsilon}{c\Delta x}. \tag{13}$$

Since infinite values of viscosity are not realistic [80], here a maximum value of τ_f (τ_f^{limit}) is set to limit the viscosity. In Section 3 below, some supplementary explanations about the choice of τ_f^{limit} are provided.

In addition, according to references [61,81], the shear rate $\dot\gamma$ is directly calculated by the distribution functions in LBM as

$$\dot\gamma = \left(S_{\alpha\beta}S_{\alpha\beta}\right)^{1/2} = \frac{3}{2\rho\tau_f c^2}\left(\sum_i f_i^{(1)} c_{i\alpha}c_{i\beta}\right)^{1/2}, \tag{14}$$

where $S_{\alpha\beta}$ is the shear rate tensor, $f_i^{(1)}$ is first order component of f_i in the Chapman–Enskog expansion; here, this term is approximated by the non-equilibrium part of f_i as

$$f_i^{(1)} \approx f_i^{neq} = f_i - f_i^{eq}. \tag{15}$$

Note that in this numerical approach only local distribution functions are used, which avoids the complex differential processes in traditional CFD methods and improves accuracy.

Combing Eqs. (6, 12, 13, 14 and 15), viscosity in LBM is obtained as

$$\tau < \tau_y: \quad \upsilon = \frac{c\Delta x}{3}\cdot\left(\tau_f^{limit} - \frac{1}{2}\right) \tag{16a}$$

$$\tau \geq \tau_y: \quad \upsilon = \frac{\tau_y}{\rho\left(S_{\alpha\beta}S_{\alpha\beta}\right)^{1/2}} + \frac{K}{\rho}\cdot\left(S_{\alpha\beta}S_{\alpha\beta}\right)^{\frac{n-1}{2}}. \tag{16b}$$

It should be noted that in order to evaluate the local shear stress, τ, the kinematic viscosity at the last time step $\nu_{(t-1)}$ is used, that is

$$\tau = \rho\nu_{(t-1)}\dot\gamma. \tag{17}$$

So far, the kinematic viscosity of a single phase viscoplastic fluid has been obtained; however, when it comes to multiphase system, special treatment at the interface is necessary. In this paper, the interface viscosity was assumed to be linearly proportional to the weight of ϕ as

$$\upsilon = \upsilon_1 + \frac{\phi - \phi_1}{\phi_2 - \phi_1}(\upsilon_2 - \upsilon_1), \tag{18}$$

where the subscripts 1 and 2 here refer to two locations close to the interface, one on each side of it; this treatment ensures the continuity of viscosity across the interface.

Therefore, substituting the viscosity calculated by Eqs. (16) and (18) into Eq. (13) allows one to determine the relaxation parameter τ_f in Eq. (6), and consequently to include viscoplastic effects into the multiphase LBM scheme.

3. Benchmarks

3.1. Validation of the LBM code for multiphase flow

The multiphase LBM code in this work is validated primarily by using parameters with exact dimensions. Here, two typical benchmark problems for two-phase flow are adopted: one is the steady droplet test, as shown in Fig. 1; and the other is a two-phase co-current flow problem, as shown in Fig. 2.

In the first case, we consider a fluid droplet with radius R surrounded by another fluid in equilibrium conditions. According to the Young-Laplace law for a 2D case, the pressure difference ΔP

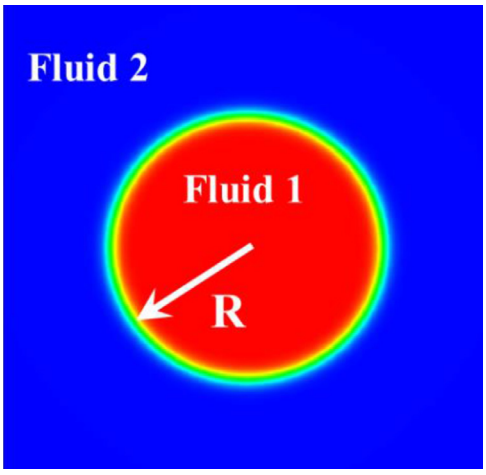

Fig. 1. Sketch of a steady droplet (Fluid 1) surrounded by another fluid (Fluid 2).

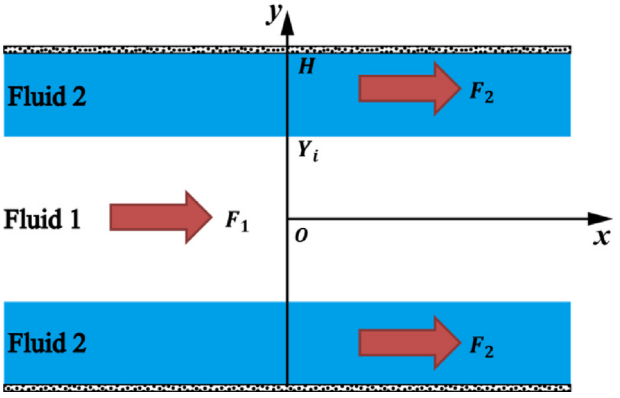

Fig. 2. Sketch of two-phase co-current flow.

across the interface is proportional to the curvature, $1/R$, when the interface tension, σ, is assigned:

$$\Delta P = \sigma / R. \tag{19}$$

Periodic boundary conditions are applied on all sides in our computation, and the fluid domain is 22 $mm \times 22$ mm, with a lattice system of 221×221. Density of fluid 1 is $\rho_1 = 1000\ kg/m^3$, for fluid 2 is $\rho_2 = 50\ kg/m^3$; kinematic viscosities of two fluids are both set as $\nu_1 = \nu_2 = 0.001 m^2/s$; interface tension is $\sigma = 0.03\ N/m$; mobility is $M = 0.01\ kg \cdot s/m^3$; and lattice velocity is $c = 100\ m/s$. The radius R varies from 2 mm to 6 mm, and the corresponding results are shown in Fig. 3, which confirms that the simulation results well satisfy the Young-Laplace law.

In the second case, illustrated schematically in Fig. 2, the parallel, co-current flow inside an axisymmetric 2D channel is considered: fluid 1 in the center driven body force F_1, while fluid 2 in the two sides driven body force F_2. The channel width is $2H$, with interface coordinates of $\pm Y_i$. When the system reaches the steady state, the following theoretical solution for the cross-sectional velocity distribution can be established as [82]

$$0 \le y < Y_i: \quad u = A_1 y^2 + C_1 \tag{20a}$$

$$Y_i \le y \le H: \quad u = A_2 y^2 + B_2 y + C_2, \tag{20b}$$

where

$$A_1 = -F_1/(2\rho_1 \nu_1) \tag{21a}$$

$$A_2 = -F_2/(2\rho_2 \nu_2) \tag{21b}$$

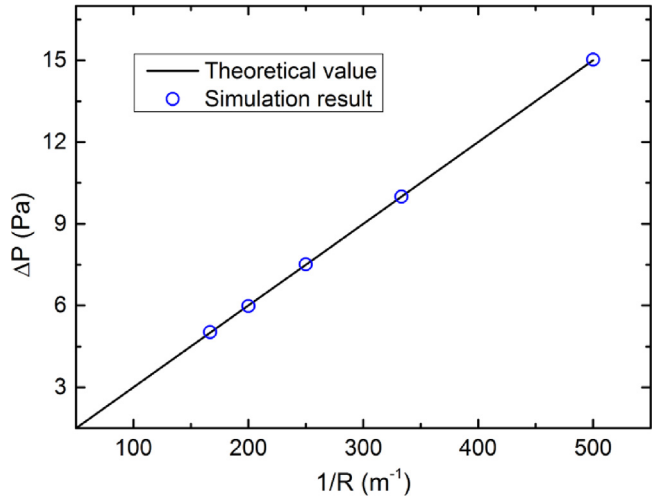

Fig. 3. Validation results of the Young-Laplace law.

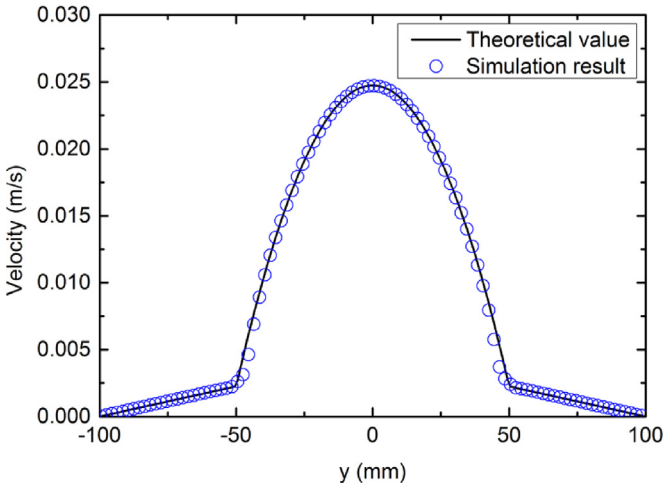

Fig. 4. Validation result of the two-phase co-current Newtonian flow.

$$B_2 = -2A_2 Y_i + 2A_1 Y_i(\rho_1 \nu_1)/(\rho_2 \nu_2) \tag{21c}$$

$$C_1 = (A_2 - A_1)Y_i^2 - B_2(H - Y_i) - A_2 H^2 \tag{21d}$$

$$C_2 = -A_2 H^2 - B_2 H. \tag{21e}$$

In the present computation, periodic boundary conditions are applied on the inlet and outlet, while for the solid boundaries at top and bottom, bounce-back rules are adopted; the fluid domain is set as 100 $mm \times 200$ mm on 101×201 lattices with $Y_i = 50mm$. Fluid densities are $\rho_1 = 1000\ kg/m^3$ and $\rho_2 = 50\ kg/m^3$; kinematic viscosities are $\nu_1 = \nu_2 = 0.01667 m^2/s$; interface tension is $\sigma = 0.03\ N/m$; mobility is $M = 0.01\ kg \cdot s/m^3$; and lattice velocity is $c = 100\ m/s$. When applying body forces of $F_1 = 15\ Pa/m$ and $F_2 = 0$, one gets the velocity profile in Fig. 4, which matches the theoretical solution well.

The above benchmark cases provide a validation of the basic multiphase LBM code ability to capture the interface dynamics and to evolve the multiphase fluid hydrodynamics.

3.2. Validation of the viscoplastic multiphase LBM model

Then, the proposed viscoplastic multiphase LBM model was validated by comparison with the problem of a two-phase co-current

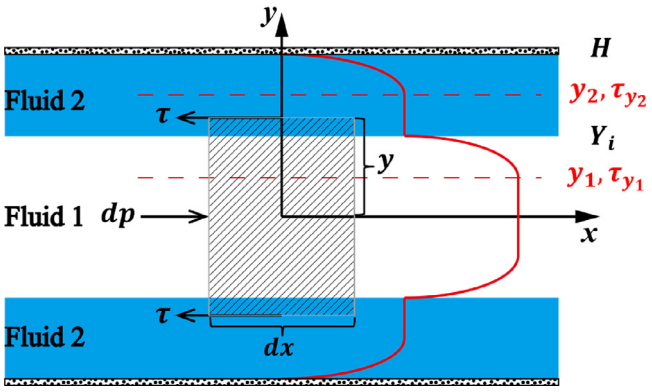

Fig. 5. Sketch of two-phase co-current Bingham flow.

Bingham flow, as shown in Fig. 5; this sketch is similar to the configuration of Fig. 2, however, the two fluids are both Bingham fluids with a same density and driven by a same pressure gradient of dp/dx, but different yield stress, τ_{y_1} and τ_{y_2}, respectively, $(\tau_{y_1} < \tau_{y_2})$. If the fluids are both partially yielded, there exist two different yield surfaces. Assuming the system is stable (i.e. the two fluids do not penetrate into each other), one can derive analytical formulations of the theoretical velocity profiles when the system is at steady-state (see the Appendix for detailed derivation).

3.2.1. LBM results versus theoretical results

In these simulations, boundary conditions were set as the same as the second case in Section 3.2 with a fluid domain of 10 $mm \times 50\ mm$ on 101×501 lattices ($H = 25mm$ and $Y_i = 12.5mm$). The physical properties of fluid 1 are: density $\rho_1 = 1005\ kg/m^3$, consistency index, $K_1 = 0.0015\ Pa \cdot s$, flow index, $n_1 = 1$, while fluid 2 has the following properties: density, $\rho_2 = 1000\ kg/m^3$, consistency index, $K_2 = 0.0075\ Pa \cdot s$, flow index, $n_2 = 1$. The interface tension between two fluids is $\sigma = 0.001\ N/m$; mobility is $M = 1.0 \times 10^{-6}\ kg \cdot s/m^3$; pressure gradient is $dp/dx = 100\ Pa/m$; lattice velocity is $c = 100\ m/s$; and the limiting relaxation parameter is $\tau_f^{limit} = 20$. Note that the densities of the two fluids are not exactly the same, to avoid a null value of the order parameter, ϕ, in the whole domain. Afterwards, different values of τ_{y_1} and τ_{y_2} were selected in order to validate the three types of velocity profiles mentioned above.

(a) Both partially yielded

Selecting $\tau_{y_1} = 0.75\ Pa$ and $\tau_{y_2} = 2\ Pa$, then the condition $\tau_{y_1} < Y_i \frac{dp}{dx} < \tau_{y_2} < H \frac{dp}{dx}$ is satisfied, and both fluids will be partially yielded. The steady state velocity profile is displayed in Fig. 6a, which shows the simulation result matches well with the theoretical profile.

(b) Only fluid 1 partially yielded

Selecting $\tau_{y_1} = 0.75\ Pa$ and $\tau_{y_2} = 3\ Pa$, then the condition $\tau_{y_1} < Y_i \frac{dp}{dx} < H \frac{dp}{dx} < \tau_{y_2}$ is satisfied, and only fluid 1 is partially yielded. The steady state result is given in Fig. 6b, and is in good agreement with the theoretical velocity profile like in the previous case.

(c) Only fluid 2 partially yielded

Selecting $\tau_{y_1} = 1.5\ Pa$ and $\tau_{y_2} = 2\ Pa$, then the condition $Y_i \frac{dp}{dx} < \tau_{y_1} < \tau_{y_2} < H \frac{dp}{dx}$ is satisfied, and only fluid 2 is partially yielded. The corresponding result is shown in Fig. 6c; in this case one can notice a small deviation at the interface between the two fluids, which is mainly caused by the small difference of the given fluid densities.

On the whole, the above comparisons provide a validation of the viscoplastic multiphase LBM model.

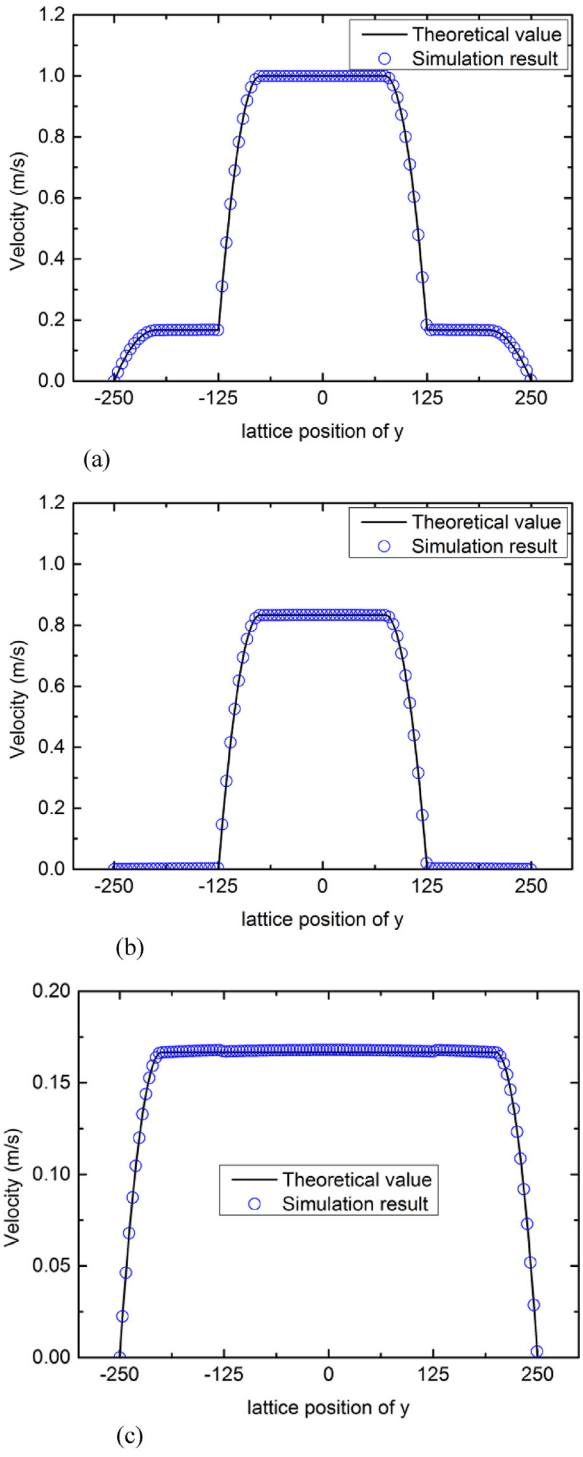

Fig. 6. Validation results of the two-phase co-current Bingham flow. (a) Both of the fluids are partially yielded. (b) Only fluid 1 is partially yielded. (c) Only fluid 2 is partially yielded.

3.2.2. Effect of the limiting relaxation parameter

The effect of the limiting relaxation parameter τ_f^{limit} is discussed. As an example, the case of both fluids yielded (Fig. 6a) is recalculated for different values of τ_f^{limit}, as shown in Fig. 7. The figure shows that once τ_f^{limit} is not too large (<100), the numerical results agree pretty well with the theoretical solution, and that when τ_f^{limit} is larger than 2, the deviation is almost invisible.

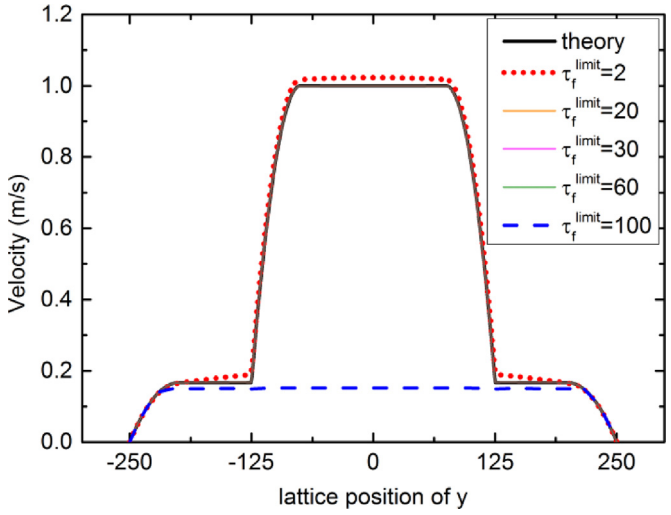

Fig. 7. Effect of limiting relaxation parameter τ_f^{limit} by comparisons with the theoretical solution. When τ_f^{limit} = 20~60, the numerical results are overlapped by the theoretical solution and not recognizable.

These results indicate that τ_f^{limit} has a significant influence on the accuracy of this model, accurate results can be obtained only if this parameter falls within an appropriate range of values. According to Eq. (16), whenever the lattice velocity c is specified, the maximum viscosity, as well as the maximum viscosity ratio, are determined by τ_f^{limit}, and larger values of τ_f^{limit} imply larger viscosity ratios. Therefore, if τ_f^{limit} is too small, the viscosity ratio is quite small too, which can't reflect adequately the infinite-viscosity behaviour and leads to wrong results. On the other hand, if τ_f^{limit} is too large, the stability of LBM is affected. In Fig. 7, $\tau_f^{limit} = 2$ corresponds to a maximum viscosity ratio of 132.7:1; this ratio is too small to ensure the uniform velocity distribution in the unyielded region caused by infinite viscosity, and also brings a small error at the interface. However, although $\tau_f^{limit} = 100$ corresponds to a sufficiently large viscosity ratio, the LBM algorithm needs a long computing time to reach steady state, and cannot return the correct result in time of relatively the same order of magnitude. On the contrary, a value of τ_f^{limit} in the range between 20 and 60 corresponds to a maximum viscosity ratio ranging between 1000:1 and 6000:1, which is able to capture adequately the infinite viscosity effect, and at the same time keeps the stability of LBM, thus leading to accurate results.

In conclusion, the guideline for choosing an appropriate value of the limiting relaxation parameter, τ_f^{limit}, is to select a large value of τ_f^{limit} to make the maximum viscosity ratio as large as possible, upon ensuring the stability of LBM. As for numerical stability and conservation in complex geometries with a variable relaxation time, a multiple-relaxation-time model [83] will be considered in future work.

4. Results and discussion

In this section, the capability of the proposed model is further investigated, with focus on three test cases: (i) single droplet falling in Bingham fluid, (ii) interaction of two droplets in Bingham fluid, (iii) sessile droplet movement in a water channel. In the first two examples, the bulk phase is viscoplastic Bingham fluid, and the results are compared with the CFD results by Potapov et al. [21]. In the last example, the droplet is viscoplastic fluid, and three droplets with different rheology are compared with each other as well as with a Newtonian droplet.

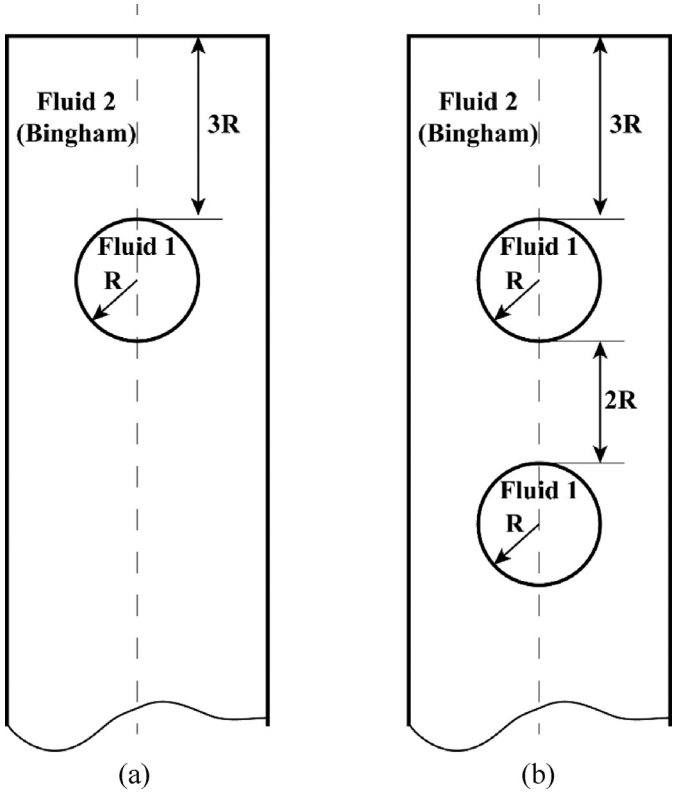

Fig. 8. Physical model of Newtonian droplet(s) falling in Bingham fluid. (a) single droplet. (b) double droplets.

4.1. Single droplet falling in Bingham fluid

The gravity-driven fall of a Newtonian droplet in a Bingham fluid medium is investigated in this section. The initial-state configuration is shown in Fig. 8a. A closed rectangular column is filled with fluid 2 (Bingham fluid of density ρ_2, consistency index K, and yield stress τ_y). In addition, an initially circular droplet (fluid 1, Newtonian fluid of density ρ_1, kinematic viscosity υ_1) with radius R is placed on the centerline. The spacing between the upper edge of the column and the droplet is 3R. This system is driven by gravity with acceleration $F_g = 9.806\ m/s^2$.

Potapov et al. [21] employed traditional CFD tools to solve this problem, with special attention to the droplet shape and to the yielded domain in the bulk fluid. Their results are used as a reference for comparison with the present calculations, although there are two differences: (i) the geometry of the column is cylindrical; (ii) results are presented in a non-dimensional form, while in the present work all parameters are dimensional. Nevertheless, if the governing non-dimensional parameters are the same, these differences will not affect significantly the shape of the yielded domain, which is the most important point for testing the present model.

The characteristic quantities used for in [21] are: $V^* = F_g R^2(\rho_1 - \rho_2)/K$ for velocity, and $t^* = K/[F_g R(\rho_1 - \rho_2)]$ for time; in addition, $\rho^* = \rho_1/\rho_2$ is the density ratio, $\lambda = \rho_1 \upsilon_1/K$ is the viscosity ratio, $Re = \rho_2 F_g R^3(\rho_1 - \rho_2)/K^3$ is the Reynolds number, $Bn = \tau_y/[F_g R(\rho_1 - \rho_2)]$ is the Bingham number, and $Ca = F_g R^2(\rho_1 - \rho_2)/\sigma$ is the Capillary number.

In the present calculations, bounce-back conditions are applied to all the boundaries, with the domain containing 201 × 1201 lattices. The values of physical parameters are chosen to match non-dimensional parameters used in [21], as shown in in Table 1, Fig. 9 displays the steady-state shape of the falling droplet and the yielded domain in the bulk phase, comparing the present results

Table 1
Parameters for simulations of a single droplet falling in a fluid medium.

Simulation parameters (present work)	Converted parameters (present work)	Simulation parameters (Ref. [21])
$\Delta x = 32.48355\ \mu m$		
$R = 20\ \Delta x$		
$\rho_1 = 1000\ kg/m^3$	$\rho^* = 1.54$	$\rho^* = 1.54$
$\rho_2 = 649.35\ kg/m^3$		
$\nu_1 = 1.0 \times 10^{-6}\ m^2/s$	$\lambda = 0.07$	$\lambda = 0.07$
$K = 0.0142857\ Pa \cdot s$	$Re = 3$	$Re = 3$
$\tau_y = 0.129565\ Pa$		
$\sigma = 2.79147 \times 10^{-5}\ N/m$	$Bn = 0.058$	$Bn = 0.058$
$M = 0.01\ kg \cdot s/m^3$		
$c = 50\ m/s$	$Ca = 51.99$	$Ca = 52$
$\tau_f^{limit} = 50$		

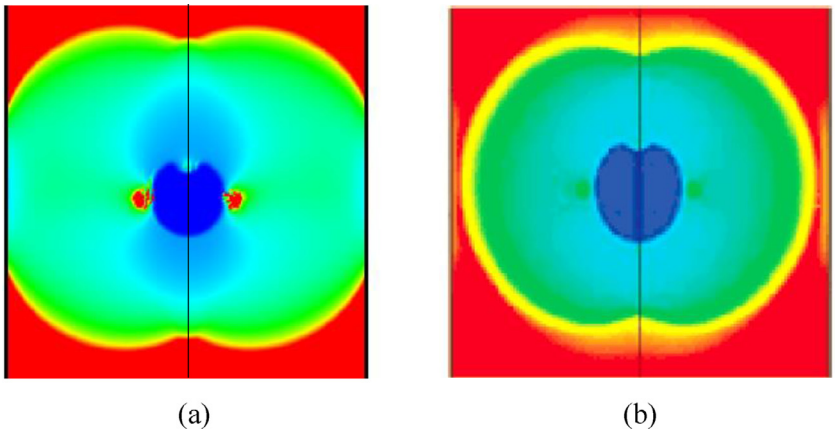

Fig. 9. Steady-state shapes of a falling droplet and the yielded domain in Bingham fluid (a) by the present simulation; (b) from the reference by Popatov et al. [21].

(a) with Potapov's (b). Viscosity is used as the contour variable for the color map, with dark blue color representing the Newtonian droplet shape. In the Bingham fluid, the unyielded region is colored in red, while the rest is the yielded domain. From this comparison, one can observe both the characteristic "apple-like" shape of the yielded domain, and a hollow region on top of the droplet; although the relative sizes of the domains are somewhat different due to the difference in geometry mentioned before, the present model is clearly able to capture the information about the yielded region.

4.2. Interaction of two droplets in Bingham fluid

In the second example, the interaction of two Newtonian droplets during free fall in a Bingham fluid medium is studied. The configuration of this problem is similar to the previous one, except for an extra droplet with the same properties and size, as shown in Fig. 8. The top of the second droplet is initially placed at the distance of 2 radii from the bottom of the first droplet. The interface tension here is set as $\sigma = 1.4515644 \times 10^{-3}\ N/m$, which leads to a Capillary number of $Ca = 1$. All the other settings are the same as in the case of single droplet free fall.

Fig. 10 illustrates the temporal evolution of the two falling droplets, and compares the present results (a) with Potapov's (b). The shapes and the yielded domains are described with the same color code of the previous example. From this figure, one can observe that the morphology resulting from the two approaches is almost the same during the entire process: before the collision, both of the upper droplets become prolate while the lower ones become oblate; then, they both merge into one larger droplet with the same shape. Simultaneously, both of the yielded domains coalesce into one, and the unyielded regions between two small droplets eventually disappear. Whilst some minor differences can still be

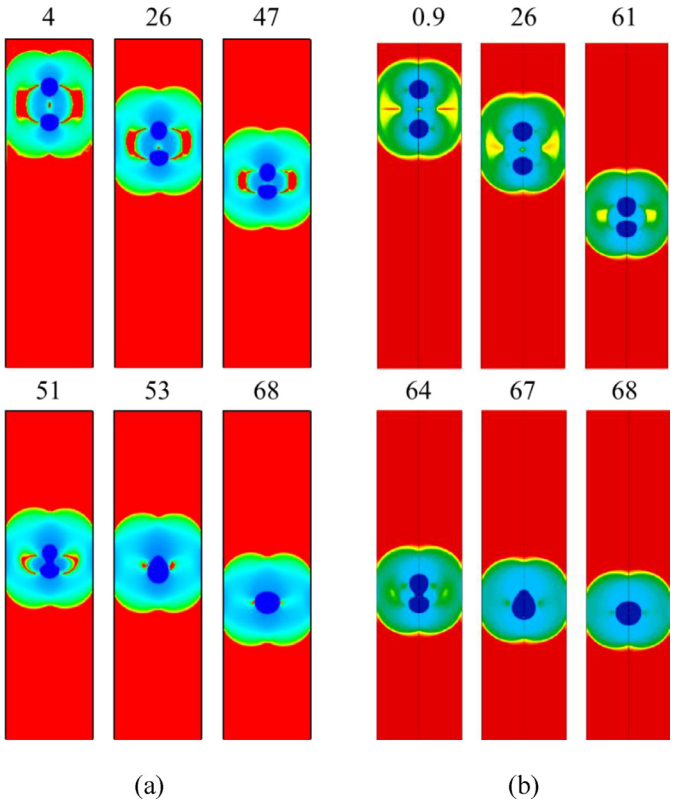

Fig. 10. Evolution of shapes and yielded domains of two droplets falling in Bingham fluid (a) by the present simulation; (b) from the reference by Popatov et al. [21].

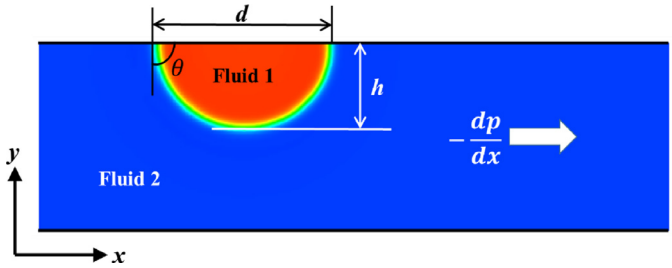

Fig. 11. Schematic of a sessile droplet movement in a straight channel filled with water.

observed, this more complex example of twin droplets falling and coalescence further demonstrates the capability of the present approach to depict the yield information in viscoplastic fluids.

4.3. Sessile droplet movement in a straight channel

Finally, the displacement of a sessile droplet in a channel filled with water was simulated. Various kinds of droplets with different rheology, including Newtonian ($\tau_y = 0$, $n = 1$), Bingham ($\tau_y > 0$, $n = 1$), Yield pseudo-plastic ($\tau_y > 0$, $n < 1$), and Yield dilatant ($\tau_y > 0$, $n > 1$) were compared with one another. This problem is relevant in the petroleum industry, since oil usually adheres to the rock surface, and water injection is often adopted to enhance oil recovery. The schematic of this problem is illustrated in Fig. 11, where fluid 2 is water, fluid 1 is the oil droplet with a lower density, θ is the contact angle, d is the base diameter, and h is the maximum height of the droplet during motion. Since gravity is considered here along the negative y direction, the oil droplet will stick to the upper wall of the channel. This system is driven by the same pressure gradient $-dp/dx$ along x direction.

To simulate this problem, we use a domain of 20 $mm \times 6$ mm on 201×61 lattices with both bounce-back boundary conditions at the top and the bottom, while the left and right sides are periodic. Initial shapes of the oil droplets are all set as the same hemisphere with a diameter of $55\Delta x$. The applied pressure gradient is $-dp/dx = 250$ Pa/m, the density of the oil is $\rho_1 = 850$ kg/m^3, the density of the water is $\rho_2 = 1000$ kg/m^3, with kinematic viscosity $\nu_2 = 1.006 \times 10^{-6}$ m^2/s, interface tension $\sigma = 0.03$ N/m, static contact angle $\theta = 90^\circ$, mobility $M = 0.0001$ $kg \cdot s/m^3$, lattice velocity $c = 100$ m/s, and the limiting relaxation parameter $\tau_f^{limit} = 200$.

Due to the complexity of its composition, the oil rheology may exhibit peculiar features. For this reason, the four typical kinds of oil droplets described above were compared, with values of the rheological parameters taken from [84]. The yield stress and consistency index were set as $\tau_y = 1.921Pa$ and $K = 0.302Pa \cdot s^n$, respectively, the flow index was $n = 1$ for Bingham oil, $n = 0.7$ for Yield pseudo-plastic oil, and $n = 1.3$ for Yield dilatant oil. For the sake of comparison with Newtonian oil, the kinematic viscosity was set as $\nu_1 = K/\rho_1 = 3.553 \times 10^{-4}$ m^2/s.

The evolution of the droplets mean velocity is given in Fig. 12. Two different stages are observed for droplets: one is the accelerating stage at the beginning; the other is an oscillating regime when the system reaches a relatively stable state. This may be mainly caused by the change of the force balance during the movement. In the horizontal (x) direction, the droplet is under the action of the driving force induced by the pressure gradient, and of the drag force caused by internal shear, viscous and interface resistance. Under given conditions, the driving force is larger than the drag force at the initial stage, and leads to the acceleration. But at a later stage, the viscous and interface resistance grows with the increasing velocity, thus the overall drag force increases and balances the driving force, as the system reaches the stable state with oscillation. However, the stable state is only in a time-averaged sense, because of small periodic fluctuations, around a constant mean value due to stick-slip motion [85]; this phenomenon is synchronous with drop shape oscillations, as shown in Fig. 13. Such small periodic deformations of the drop shape in turn change the advancing and receding contact angles, which can be observed clearly in Fig. 13c, for example. Because the interface tension is always tangent to the drop-fluid interface, the change in dynamic contact angles results into fluctuations of its component in the x direction; consequently, the resultant force fluctuates, inducing the observed stick-slip motion.

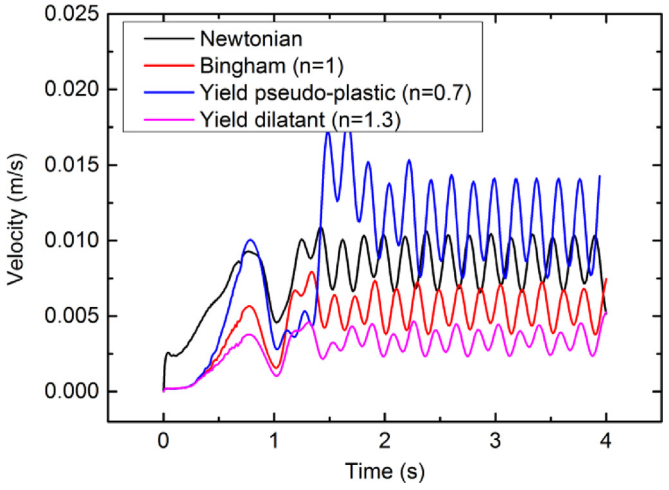

Fig. 12. Comparisons of the mean velocity evolution of oil droplets with different rheology.

In the early stage, the Newtonian droplet accelerates immediately and reaches the largest velocity; however, for all viscoplastic droplets the acceleration ramp is delayed, which is mainly caused by the existence of yield stress. In fact, as the external flow begins to exert a drag on the drop, the induced shear stresses are smaller than the yield stress. Thus, the drop acceleration starts only when the shear stress exceeds the yield stress.

The relative magnitudes of velocity change in the late stage, the fastest being the yield-stress pseudo-plastic droplet, followed in descending order by the Newtonian droplet, the Bingham droplet, and the Yield dilatant droplet. This result seems quite reasonable for the following reasons: in the Bingham droplet, although the flow index is the same as in the Newtonian droplet, the apparent viscosity is always larger under the same shear rate, according to Eq. (12b), thus the drag force is larger and leads to a smaller velocity; compared with the Bingham droplet, the flow index of the Yield dilatant droplet is greater than one, thus viscosity and the induced drag force increase when the drop velocity is increased, and as a consequence this drop exhibits the smallest velocity; unlike with Yield dilatant droplet, since $n < 1$, the viscosity of Yield pseudo-plastic droplet decreases during the acceleration and the extent may even neutralize the extra viscosity induced by τ_y, and under such condition, the Yield pseudo-plastic droplet moves with a speed higher than the Newtonian droplet. In summary, the effectivity of the proposed model for distinguishing various kinds of viscoplastic fluids is well examined by this example.

5. Conclusions

In this paper, a LBM scheme based on phase-field method for multiphase Newtonian fluids is extended to viscoplastic fluids, by applying the Herschel-Bulkley constitutive relationship. The multiphase LBM code and the proposed viscoplastic multiphase

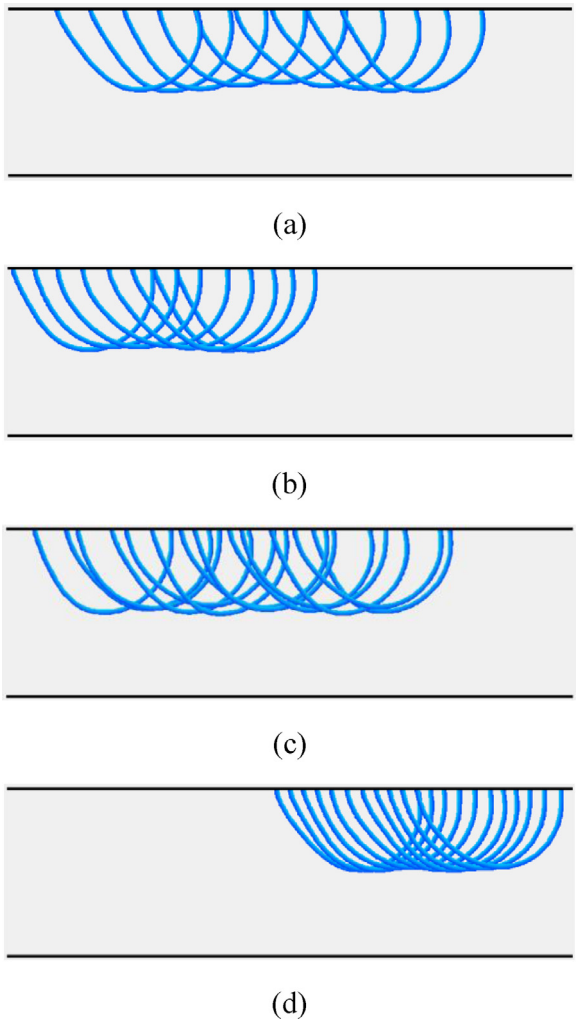

Fig. 13. Interface profile evolution of different droplets in the late stage. Droplets move from left to right: (a) Newtonian droplet ($t = 2.6$–$3.9\,s$); (b) Bingham droplet ($t = 3.8$–$5.0\,s$); (c) Yield pseudo-plastic droplet ($t = 2.4$–$3.4\,s$); (d) Yield dilatant droplet ($t = 2.4$–$3.9\,s$).

LBM model are initially validated against cases with exact analytical solutions. In all cases, the LBM results are in good agreements with the theoretical data, which validates the accuracy of the proposed model in simulating multiphase viscoplastic fluids with high density ratios.

Thereafter, the proposed model is applied to three different examples of multiphase viscoplastic flows. In the first two examples, relative to droplet(s) falling in a Bingham fluid medium, the present results are compared with a CFD simulation taken from the literature; despite some minor differences in geometry, the resulting shapes of the droplets and of the yielded domains are quite similar. Finally, sessile droplets motion in a straight channel is simulated in the case of a Newtonian droplet, a Bingham droplet, a Yield pseudo-plastic droplet, and Yield dilatant droplet. The corresponding results indicate significant but reasonable differences among the behaviors of these droplets. In conclusion, by these three examples, the capability and effectivity of this model is further illustrated. Although only 2D cases are presented in this work for better demonstration, it is easy to extend to 3D problems. The application to more complex geometries is also expected in future work.

Acknowledgements

This work is financially supported by the NSF grant of China (No. 51176089, U1562217), National Science and Technology Major Project on Oil and Gas (No.2016ZX05013001), PetroChina Innovation Foundation (No. 2015D-5006-0201) and the Tsinghua University Initiative Scientific Research Program (No. 2014z22074). We thank Prof. Shu, C. and Dr. Shao, J.Y., Dr. Liu Q.J. and Dr. Lei Z.D. for their helpful discussion.

Appendix. Theoretical solutions for the stable two-phase co-current Bingham flow

Here we present the details of the derivation of theoretical velocity profiles for the stable two-phase co-current Bingham flow. Frigaard [9] has derived the analytical solution for this problem, and pointed out that there exist three typical kinds of velocity profiles when given different shear conditions. These results were presented in a dimensionless form by using the steady state average velocity. Since this velocity is unknown at the beginning of the numerical modeling, establishing an accurate comparison is not easy. As a consequence, we rebuild a group of dimensional results here. Because of the problem symmetry, only the positive half of the y-axis ($y \geq 0$) is considered in the following derivation.

According to Eq. (11), the constitutive equation of Bingham fluid 1 is

$$\tau \leq \tau_{y_1}: \quad \dot{\gamma} = 0 \tag{A1a}$$

$$\tau > \tau_{y_1}: \quad \tau = \tau_{y_1} - K_1\dot{\gamma}. \tag{A1b}$$

Similarly, for fluid 2

$$\tau \leq \tau_{y_2}: \quad \dot{\gamma} = 0 \tag{A2a}$$

$$\tau > \tau_{y_2}: \quad \tau = \tau_{y_2} - K_2\dot{\gamma}. \tag{A2b}$$

Since stable flow is assumed, the y-velocity component is zero, then the shear rate $\dot{\gamma}$ is only determined by x-velocity component u as

$$\dot{\gamma} = \frac{du}{dy}. \tag{A3}$$

Consider a symmetrical control volume alone the centerline with size of $dx \times 2y \times 1$, corresponding to the shaded area in Fig. 5. This control volume is subject to the shear stress τ on top and bottom, plus a normal stress along the flow direction; they are balanced at steady state as

$$2\tau \cdot dx \cdot 1 = \frac{dp}{dx} \cdot dx \cdot 2y \cdot 1. \tag{A4}$$

Then the correlation between the shear stress τ and coordinate y is obtained as

$$\tau = \frac{dp}{dx} \cdot y. \tag{A5}$$

As it is well known, the shear stress increases from the centerline to the wall for pressure driven flows, due to the shearing effect of the solid wall. In addition with the assumption of $\tau_{y_1} < \tau_{y_2}$, the relation of two yield positions is $y_1 < y_2$, and

$$y = y_1: \quad \tau = \tau_{y_1} \quad \Rightarrow \quad y_1 = \tau_{y_1} / \frac{dp}{dx} \tag{A6a}$$

$$y = y_2: \quad \tau = \tau_{y_2} \quad \Rightarrow \quad y_2 = \tau_{y_2} / \frac{dp}{dx}. \tag{A6b}$$

By using these two yield positions, we can divide three types of cross-sectional velocity profiles and give the corresponding theoretical results as follows.

(a) Both partially yielded

If $0 < y_1 < Y_i < y_2 < H$ (i.e. $\tau_{y_1} < Y_i\frac{dp}{dx} < \tau_{y_2} < H\frac{dp}{dx}$), y_1 and y_2 exist, and both of the fluids will be partially yielded.

By substituting Eq. (A3) into Eqs. (A1 and A2), we get

$$y_1 \le y \le Y_i: \quad \tau = \tau_{y_1} - K_1\frac{du}{dy} \tag{A7a}$$

$$y_2 \le y \le H: \quad \tau = \tau_{y_2} - K_2\frac{du}{dy}. \tag{A7b}$$

Integration of the above equations leads to

$$y_1 \le y \le Y_i: \quad u = \left(-\frac{1}{2}\frac{dp}{dx}y^2 + \tau_{y_1}y + C_1\right)/K_1 \tag{A8a}$$

$$y_2 \le y \le H: \quad u = \left(-\frac{1}{2}\frac{dp}{dx}y^2 + \tau_{y_2}y + C_2\right)/K_2, \tag{A8b}$$

where C_1 and C_2 are constants. Applying the boundary condition $u = 0$ at $y = H$ to Eq. (A8b), C_2 is derived as

$$C_2 = \frac{1}{2}\frac{dp}{dx}H^2 - \tau_{y_2}H. \tag{A9}$$

In the region of $Y_i < y < y_2$, $\tau < \tau_{y_2}$, and fluid 2 does not yield with a uniform velocity of u_2. Combing with Eq. (A8b) and using the continuity at $y = y_2$, u_2 is obtained as

$$Y_i \le y < y_2: \quad u = u_2 = \left(\frac{\tau_{y_2}^2}{2\frac{dp}{dx}} + C_2\right)/K_2. \tag{A10}$$

Substituting Eq. (A10) into Eq. (A8a) and using the continuity at $y = Y_i$, C_1 is derived as

$$C_1 = K_1u_2 + \frac{1}{2}\frac{dp}{dx}Y_i^2 - \tau_{y_1}Y_i. \tag{A11}$$

Accordingly, in the region of $0 \le y < y_1$, $\tau < \tau_{y_1}$, and fluid 1 does not yield with a uniform velocity of u_1. Combing with Eq. (A8a) and using the continuity at $y = y_1$, u_1 is obtained as

$$0 \le y < y_1: \quad u = u_1 = \left(\frac{\tau_{y_1}^2}{2\frac{dp}{dx}} + C_1\right)/K_1. \tag{A12}$$

To sum up, the theoretical velocity distribution under the shear condition of $\tau_{y_1} < Y_i\frac{dp}{dx} < \tau_{y_2} < H\frac{dp}{dx}$ is

$$0 \le y \le y_1: \quad u = u_1 = \left(\frac{\tau_{y_1}^2}{2\frac{dp}{dx}} + K_1u_2 + \frac{1}{2}\frac{dp}{dx}Y_i^2 - \tau_{y_1}Y_i\right)/K_1 \tag{A13a}$$

$$y_1 < y < Y_i: \quad u = \left(-\frac{1}{2}\frac{dp}{dx}y^2 + \tau_{y_1}y + K_1u_2 + \frac{1}{2}\frac{dp}{dx}Y_i^2 - \tau_{y_1}Y_i\right)/K_1 \tag{A13b}$$

$$Y_i \le y \le y_2: \quad u = u_2 = \left(\frac{\tau_{y_2}^2}{2\frac{dp}{dx}} + \frac{1}{2}\frac{dp}{dx}H^2 - \tau_{y_2}H\right)/K_2 \tag{A13c}$$

$$y_2 < y \le H: \quad u = \left(-\frac{1}{2}\frac{dp}{dx}y^2 + \tau_{y_2}y + \frac{1}{2}\frac{dp}{dx}H^2 - \tau_{y_2}H\right)/K_2. \tag{A13d}$$

(b) Only fluid 1 partially yielded

If $0 < y_1 < Y_i < H < y_2$ (i.e. $\tau_{y_1} < Y_i\frac{dp}{dx} < H\frac{dp}{dx} < \tau_{y_2}$), y_2 doesn't exist, and only fluid 1 will be partially yielded.

Likewise, in the region of fluid 1, Eqs. (A7a, A8a and A12) remain the same. While in the region of $Y_i \le y \le H$, $\tau < \tau_{y_2}$, thus the whole fluid 2 does not yield. Using the boundary condition $u = 0$ at $y = H$, we get

$$Y_i \le y \le H: \quad u = u_2 = 0. \tag{A14}$$

By substituting it into Eq. (A11), C_1 here is derived as

$$C_1 = \frac{1}{2}\frac{dp}{dx}Y_i^2 - \tau_{y_1}Y_i. \tag{A15}$$

Further substituting Eq. (A15) into Eqs. (A8a and A12), the theoretical velocity distribution under the shear condition of $\tau_{y_1} < Y_i\frac{dp}{dx} < H\frac{dp}{dx} < \tau_{y_2}$ is obtained as

$$0 \le y \le y_1: \quad u = u_1 = \left(\frac{\tau_{y_1}^2}{2\frac{dp}{dx}} + \frac{1}{2}\frac{dp}{dx}Y_i^2 - \tau_{y_1}Y_i\right)/K_1 \tag{A16a}$$

$$y_1 < y < Y_i: \quad u = \left(-\frac{1}{2}\frac{dp}{dx}y^2 + \tau_{y_1}y + \frac{1}{2}\frac{dp}{dx}Y_i^2 - \tau_{y_1}Y_i\right)/K_1 \tag{A16b}$$

$$Y_i \le y \le H: \quad u = u_2 = 0. \tag{A16c}$$

(c) Only fluid 2 partially yielded

If $0 < Y_i < y_1 < y_2 < H$ (i.e. $Y_i\frac{dp}{dx} < \tau_{y_1} < \tau_{y_2} < H\frac{dp}{dx}$), y_1 doesn't exist, and only fluid 2 will be partially yielded.

Similarly, in the region of fluid 2, Eqs. (A7b, A8b, A9 and A10) remain the same. While in the region of $0 \le y \le Y_i$, $\tau < \tau_{y_1}$, thus the whole fluid 1 does not yield. Using the continuity at $y = Y_i$, we get

$$0 \le y \le Y_i: \quad u = u_1 = u_2 = \left(\frac{\tau_{y_2}^2}{2\frac{dp}{dx}} + C_2\right)/K_2. \tag{A17}$$

Therefore, the theoretical velocity distribution under the shear condition of $Y_i\frac{dp}{dx} < \tau_{y_1} < \tau_{y_2} < H\frac{dp}{dx}$ is

$$0 \le y \le y_2: \quad u = u_1 = u_2 = \left(\frac{\tau_{y_2}^2}{2\frac{dp}{dx}} + \frac{1}{2}\frac{dp}{dx}H^2 - \tau_{y_2}H\right)/K_2 \tag{A18a}$$

$$y_2 < y \le H: \quad u = \left(-\frac{1}{2}\frac{dp}{dx}y^2 + \tau_{y_2}y + \frac{1}{2}\frac{dp}{dx}H^2 - \tau_{y_2}H\right)/K_2. \tag{A18b}$$

References

[1] H.A. Barnes, The yield stress—a review or '$\pi\alpha\nu\tau\alpha\ \rho\varepsilon\iota$' —everything flows? J. Non-Newtonian Fluid Mech. 81 (1999) 133–178.

[2] J. Jung, R.W. Lyczkowski, C.B. Panchal, A. Hassanein, Multiphase hemodynamic simulation of pulsatile flow in a coronary artery, J. Biomech. 39 (2006) 2064–2073.

[3] Y.H. Kim, P.J. VandeVord, J.S. Lee, Multiphase non-Newtonian effects on pulsatile hemodynamics in a coronary artery, Int. J. Numer. Methods Fluids 58 (2008) 803–825.

[4] M.S. Cho, Y.H. Cho, H.J. Choi, M.S. Jhon, Synthesis and electrorheological characteristics of polyaniline-coated poly (methyl methacrylate) microsphere: size effect, Langmuir 19 (2003) 5875–5881.

[5] S. Pelipenko, I.A. Frigaard, Visco-plastic fluid displacements in near-vertical narrow eccentric annuli: prediction of travelling-wave solutions and interfacial instability, J. Fluid Mech. 520 (2004) 343–377.

[6] S.M. Taghavi, K. Alba, M. Moyers-Gonzalez, I.A. Frigaard, Incomplete fluid-fluid displacement of yield stress fluids in near-horizontal pipes: Experiments and theory, J. Non-Newtonian Fluid Mech. 167 (2012) 59–74.

[7] O.M. Lavrenteva, A. Nir, Viscoplastic flows with free boundaries and interfaces, Rev. Chem. Eng. 26 (2010) 149.

[8] E. Comparini, P. Mannucci, Flow of a Bingham fluid in contact with a Newtonian fluid, J. Math. Anal. Appl. 227 (1998) 359–381.

[9] I.A. Frigaard, Super-stable parallel flows of multiple visco-plastic fluids, J. Non-Newtonian Fluid Mech. 100 (2001) 49–75.

[10] N. Dubash, I.A. Frigaard, Propagation and stopping of air bubbles in Carbopol solutions, J. Non-Newtonian Fluid Mech. 142 (2007) 123–134.

[11] D. Sikorski, H. Tabuteau, J.R. de Bruyn, Motion and shape of bubbles rising through a yield-stress fluid, J. Non-Newtonian Fluid Mech. 159 (2009) 10–16.

[12] K. Terasaka, H. Tsuge, Bubble formation at a nozzle submerged in viscous liquids having yield stress, Chem. Eng. Sci. 56 (2001) 3237–3245.

[13] Y. Holenberg, O.M. Lavrenteva, A. Nir, Interaction of viscous drops in a yield stress material, Rheologica Acta 50 (2011) 375–387.
[14] O.M. Lavrenteva, Y. Holenberg, A. Nir, Motion of viscous drops in tubes filled with yield stress fluid, Chem. Eng. Sci. 64 (2009) 4772–4786.
[15] M. Aminzadeh, A. Maleki, B. Firoozabadi, H. Afshin, On the motion of Newtonian and non-Newtonian liquid drops, Scientia Iranica 19 (2012) 1265–1278.
[16] G. German, V. Bertola, Formation of viscoplastic drops by capillary breakup, Phys. Fluids 22 (2010) 033101.
[17] G. German, V. Bertola, G. German, V. Bertola, The free-fall of viscoplastic drops, J. Non-Newtonian Fluid Mech. 165 (2010) 825–828.
[18] G. German, V. Bertola, Impact of shear-thinning and yield-stress drops on solid substrates, J. Phys. 21 (2009) 375111.
[19] M.K. Tripathi, K.C. Sahu, G. Karapetsas, O.K. Matar, Bubble rise dynamics in a viscoplastic material, J. Non-Newtonian Fluid Mech. 222 (2015) 217–226.
[20] Y. Dimakopoulos, J. Tsamopoulos, Transient displacement of a viscoplastic material by air in straight and suddenly constricted tubes, J. Non-Newtonian Fluid Mech. 112 (2003) 43–75.
[21] A. Potapov, R. Spivak, O.M. Lavrenteva, A. Nir, Motion and deformation of drops in Bingham fluid, Ind. Eng. Chem. Res. 45 (2006) 6985–6995.
[22] J.P. Singh, M.M. Denn, Interacting two-dimensional bubbles and droplets in a yield-stress fluid, Phys. Fluids 20 (2008) 040901.
[23] Y. Dimakopoulos, M. Pavlidis, J. Tsamopoulos, Steady bubble rise in Herschel-Bulkley fluids and comparison of predictions via the Augmented Lagrangian Method with those via the Papanastasiou model, J. Non-Newtonian Fluid Mech. 200 (2013) 34–51.
[24] I. Smagin, M. Pathak, O.M. Lavrenteva, A. Nir, Motion and shape of an axisymmetric viscoplastic drop slowly falling through a viscous fluid, Rheolog. Acta 50 (2011) 361–374.
[25] R. Govindarajan, K.C. Sahu, Instabilities in viscosity-stratified flow, Ann. Rev. Fluid Mech. 46 (2014) 331–353.
[26] C.K. Aidun, J.R. Clausen, Lattice-Boltzmann method for complex flows, Ann. Rev. Fluid Mech. 42 (2010) 439–472.
[27] S. Chen, G.D. Doolen, Lattice Boltzmann method for fluid flows, Ann. Rev. Fluid Mech. 30 (1998) 329–364.
[28] S. Succi, The Lattice Boltzmann Equation For Fluid Dynamics And Beyond, Oxford University Press, Oxford, 2001.
[29] G. Breyiannis, D. Valougeorgis, Lattice kinetic simulations in three-dimensional magnetohydrodynamics, Phys. Rev. E 69 (2004) 065702.
[30] M. Wang, Structure effects on Electro-osmosis in microporous media, J. Heat Transf. 134 (2012) 051020.
[31] M. Wang, Q. Kang, Electrokinetic transport in microchannels with random roughness, Anal. Chem. 81 (2009) 2953–2961.
[32] M. Wang, N. Pan, Predictions of effective physical properties of complex multiphase materials, Mater. Sci. Eng. 63 (2008) 1–30.
[33] C. Xie, J. Wang, D. Wang, N. Pan, M. Wang, Lattice Boltzmann modeling of thermal conduction in composites with thermal contact resistance, Commun. Comput. Phys. 17 (2015) 1037–1055.
[34] X. He, N. Li, Lattice Boltzmann simulation of electrochemical systems, Comput. Phys. Commun. 129 (2000) 158–166.
[35] H. Liu, Q. Kang, C.R. Leonardi, B.D. Jones, S. Schmieschek, Narv, J.R.Williams, A.J. Valocchi, J. Harting, Multiphase lattice Boltzmann simulations for porous media applications - a review, (2014) arXiv:1404.7523.
[36] D. Grunau, S. Chen, K. Eggert, A lattice Boltzmann model for multiphase fluid flows, Phys. Fluids A 5 (1993) 2557–2562.
[37] A.K. Gunstensen, D.H. Rothman, Lattice-Boltzmann studies of immiscible two-phase flow through porous media, J. Geophys. Res. 98 (1993) 6431–6441.
[38] A.K. Gunstensen, D.H. Rothman, S. Zaleski, G. Zanetti, Lattice Boltzmann model of immiscible fluids, Phys. Rev. A 43 (1991) 4320–4327.
[39] D. Rothman, J. Keller, Immiscible cellular-automaton fluids, J.Stat. Phys. 52 (1988) 1119–1127.
[40] X. Shan, H. Chen, Lattice Boltzmann model for simulating flows with multiple phases and components, Phys. Rev. Lett. 47 (1993) 1815–1819.
[41] M.R. Swift, W.R. Osborn, J.M. Yeomans, Lattice Boltzmann simulation of nonideal fluids, Phys. Rev. Lett. 75 (1995) 830–833.
[42] X. He, S. Chen, G.D. Doolen, A novel thermal model for the lattice Boltzmann method in incompressible limit, J. Comput. Phys. 146 (1998) 282–300.
[43] X. He, S. Chen, R. Zhang, A lattice Boltzmann scheme for incompressible multiphase flow and its application in simulation of Rayleigh-Taylor instability, J. Comput. Phys. 152 (1999) 642–663.
[44] J.W. Cahn, Free energy of a nonuniform system. II. thermodynamic basis, J. Chem. Phys. 30 (1959) 1121–1124.
[45] J.W. Cahn, J.E. Hilliard, Free energy of a nonuniform system. I. interfacial free energy, J. Chem. Phys. 28 (1958) 258–267.
[46] J.W. Cahn, J.E. Hilliard, Free energy of a nonuniform system. III. nucleation in a two-component incompressible fluid, J. Chem. Phys. 31 (1959) 688–699.
[47] A. Mazloomi M, S.S. Chikatamarla, I.V. Karlin, Entropic Lattice Boltzmann Method for Multiphase Flows, Phys. Rev. Lett. 114 (2015) 174502.
[48] A. Mazloomi M, S.S. Chikatamarla, I.V. Karlin, Entropic lattice Boltzmann method for multiphase flows: Fluid-solid interfaces, Phys.l Rev. E 92 (2015) 023308.
[49] T. Inamuro, T. Ogata, S. Tajima, N. Konishi, A lattice Boltzmann method for incompressible two-phase flows with large density differences, 198 (2004) 628–644.
[50] T. Lee, C.-L. Lin, A stable discretization of the lattice Boltzmann equation for simulation of incompressible two-phase flows at high density ratio, J. Comput. Phys. 206 (2005) 16–47.
[51] K. Connington, T. Lee, Lattice Boltzmann simulations of forced wetting transitions of drops on superhydrophobic surfaces, J. Comput. Phys. 250 (2013) 601–615.
[52] T. Lee, L. Liu, Lattice Boltzmann simulations of micron-scale drop impact on dry surfaces, J. Comput. Phys. 229 (2010) 8045–8063.
[53] H.W. Zheng, C. Shu, Y.T. Chew, A lattice Boltzmann model for multiphase flows with large density ratio, J. Comput. Phys. 218 (2006) 353–371.
[54] C. Xie, J. Zhang, V. Bertola, M. Wang, Droplet evaporation on a horizontal substrate under gravity field by mesoscopic modeling, J. Coll. Interf. Sci. 463 (2016) 317–323.
[55] M.H. Rahimian, A. Fakhari, Phase-field modeling by the method of lattice Boltzmann equations, Phys. Rev. E 81 (2010) 036707.
[56] J.Y. Shao, C. Shu, H.B. Huang, Y.T. Chew, Free-energy-based lattice Boltzmann model for the simulation of multiphase flows with density contrast, Phys. Rev. E 89 (2014) 033309.
[57] T.N. Phillips, G.W. Roberts, Lattice Boltzmann models for non-Newtonian flows, IMA J. Appl. Math. 76 (2011) 790–816.
[58] S. Gabbanelli, G. Drazer, J. Koplik, Lattice Boltzmann method for non-Newtonian (power-law) fluids, Phys. Rev. E 72 (2005) 046312.
[59] J. Boyd, J. Buick, S. Green, A second-order accurate lattice Boltzmann non-Newtonian flow model, J. Phys. A 39 (2006) 14241.
[60] G. Pontrelli, S. Ubertini, S. Succi, The unstructured lattice Boltzmann method for non-Newtonian flows, J. Stat. Mech. (2009) P06005.
[61] S. Chen, X. He, V. Bertola, M. Wang, Electro-osmosis of non-Newtonian fluids in porous media using lattice Poisson-Boltzmann method, J. Coll. Interf. Sci. 436 (2014) 186–193.
[62] I. Ispolatov, M. Grant, Lattice Boltzmann method for viscoelastic fluids, Phys. Rev. E 65 (2002) 056704.
[63] P. Lallemand, D.D. Humieres, L.-S. Luo, R. Rubinstein, Theory of the lattice Boltzmann method: three-dimensional model for linear viscoelastic fluids, Phys. Rev. E 67 (2003) 021203.
[64] M. Ohta, T. Nakamura, Y. Yoshida, Y. Matsukuma, Lattice Boltzmann simulations of viscoplastic fluid flows through complex flow channels, J. Non-Newtonian Fluid Mech. 166 (2011) 404–412.
[65] A. Vikhansky, Lattice-Boltzmann method for yield-stress liquids, J. Non-Newtonian Fluid Mech. 155 (2008) 95–100.
[66] J.J. Derksen, Simulations of mobilization of Bingham layers in a turbulently agitated tank, J. Non-Newtonian Fluid Mech. 191 (2013) 25–34.
[67] X. Frank, H.Z. Li, Complex flow around a bubble rising in a non-Newtonian fluid, Phys. Rev. E 71 (2005) 036309.
[68] X. Frank, H.Z. Li, Negative wake behind a sphere rising in viscoelastic fluids: a lattice Boltzmann investigation, Phys. Rev. E 74 (2006) 056307.
[69] J. Onishi, Y. Chen, H. Ohashi, Dynamic simulation of multi-component viscoelastic fluids using the lattice Boltzmann method, Phys. A 362 (2006) 84–92.
[70] M. Yoshino, Y. Toriumi, M. Arai, Lattice Boltzmann simulation of two-phase viscoelastic fluid flows, J. Comput. Sci. Technol. 2 (2008) 330–340.
[71] Y. Shi, G.H. Tang, Lattice Boltzmann Simulation of Droplet Formation in Non-Newtonian Fluids, Commun. Comput. Phys. 17 (2015) 1056–1072.
[72] C. Xie, J. Zhang, M. Wang, Lattice Boltzmann modeling of non-Newtonian multiphase fluid displacement, Chin. J. Comput. Phys. 33 (2016) 0147.
[73] P.A.P. Swain, G. Karapetsas, O.K. Matar, K.C. Sahu, Numerical simulation of pressure-driven displacement of a viscoplastic material by a Newtonian fluid using the lattice Boltzmann method, Eur. J. Mechanics - B/Fluids 49 (2015) 197–207.
[74] C.W. Hirt, B.D. Nichols, Volume of fluid (VOF) method for the dynamics of free boundaries, J. Comput. Phys. 39 (1981) 201–225.
[75] S. Osher, R.P. Fedkiw, Level set methods: an overview and some recent results, J. Comput. Phys. 169 (2001) 463–502.
[76] S. Tanguy, A. Berlemont, Application of a level set method for simulation of droplet collisions, Int. J. Multiphase Flow 31 (2005) 1015–1035.
[77] D.M. Anderson, G.B. McFadden, A.A. Wheeler, Diffuse-interface methods in fluid mechanics, Ann. Rev. Fluid Mech. 30 (1998) 139–165.
[78] J.J. Huang, C. Shu, Y.T. Chew, Mobility-dependent bifurcations in capillarity-driven two-phase fluid systems by using a lattice Boltzmann phase-field model, Int. J. Numer. Methods Fluids 60 (2009) 203–225.
[79] W.H. Herschel, R. Bulkley, Konsistenzmessungen von Gummi-Benzoll?sungen, Kolloid-Zeitschrift 39 (1926) 291–300.
[80] P. Coussot, Yield stress fluid flows: A review of experimental data, J. Non-Newtonian Fluid Mech. 211 (2014) 31–49.
[81] A.M.M. Artoli, Mesoscopic Computational Haemodynamics, University van Amsterdam, Amsterdam, Netherlands, 2003.
[82] H. Huang, X.-Y. Lu, Relative permeabilities and coupling effects in steady-state gas-liquid flow in porous media: A lattice Boltzmann study, Phys. Fluids 21 (2009) 092104.
[83] Z.H. Chai, B.C. Shi, Z.L. Guo, F.M. Rong, Multiple-relaxation-time lattice Boltzmann model for generalized Newtonian fluid flows, J. Non-Newtonian Fluid Mech. 166 (2011) 332–342.
[84] T.F. Al-Fariss, K.L. Pinder, Flow of a shear-thinning liquid with yield stress through porous media, SPE J. (1984) 13840.
[85] D. Ferraro, P. Fantinel, M. Pierno, G. Mistura, G. Amati, L. Biferale, M. Sbragaglia, S. Varagnolo, Stick-slip sliding of water drops on chemically heterogeneous surfaces, Phys. Rev. Lett. 111 (2013) 066101.